PHYSICAL REVIEW E **75**, 036402 (2007)

Production of a monoenergetic electron bunch in a self-injected laser-wakefield accelerator

C.-L. Chang,[1] C.-T. Hsieh,[1] Y.-C. Ho,[1] Y.-S. Chen,[1,2] J.-Y. Lin,[2] J. Wang,[1,3,4,*] and S.-Y. Chen[1,3,†]
[1]*Institute of Atomic and Molecular Sciences, Academia Sinica, Taipei 106, Taiwan*
[2]*Department of Physics, National Chung Cheng University, Chia-Yi 621, Taiwan*
[3]*Department of Physics, National Central University, Jhong-Li 320, Taiwan*
[4]*Department of Physics, National Taiwan University, Taipei, 106, Taiwan*

(Received 25 September 2006; published 7 March 2007)

Production of a monoenergetic electron bunch in a self-injected laser-wakefield accelerator is investigated with a tomographic method which resolves the electron injection and acceleration processes. It is found that all the electrons in the monoenergetic electron bunch are injected at the same location in the plasma column and then accelerated with an acceleration gradient exceeding 2 GeV/cm. The injection position shifts with the position of pump-pulse focus, and no significant deceleration is observed for the monoenergetic electron bunch after it reaches the maximum energy. The results are consistent with the model of transverse wave breaking and beam loading for the injection of monoenergetic electrons. The tomographic method adds a crucial dimension to the whole array of existing diagnostics for laser beams, plasma waves, and electron beams. With this method the details of the underlying physical processes in laser-plasma interactions can be resolved and compared directly to particle-in-cell simulations.

DOI: 10.1103/PhysRevE.75.036402 PACS number(s): 52.38.Kd, 52.38.Hb, 52.50.Jm, 52.38.Mf

I. INTRODUCTION

Laser-wakefield acceleration (LWFA) [1] of electrons in a plasma has the potential of becoming the next-generation electron accelerator [2] because of the extremely large acceleration gradient and compact size. The acceleration gradient of relativistic plasma wave can reach several GeV/cm, which is approximately three orders of magnitude greater than that of the conventional radio-frequency linac limited by breakdown occurring on the wall of the structure [3]. In the early stage of development electrons produced by laser-wakefield accelerators have an energy spectrum of quasi-Maxwellian distribution and a maximum energy of a few hundreds MeV [4,5]. These continuum electrons are trapped from the background plasma continuously rather than being injected at a specific space and time. Such a continuum energy distribution poses serious limitations on applications. Recently production of well-collimated electron beam with up to GeV energy and narrow energy spread was achieved by many groups using a laser pulse in either a bare gas jet [6–13] or a preformed plasma waveguide [14–17]. With this advancement the laser-wakefield accelerator is now brought closer to being an alternative to the conventional accelerator for practical applications [18–21].

The processes of self-injection and acceleration of the monoenergetic electron beam have been studied by particle-in-cell simulations and theoretical analyses [22–28]. According to these works the basic physical picture is as follows. When an intense laser pulse propagates in a plasma, it drives a plasma wave and at the same time undergoes self-focusing and longitudinal compression, thus creating a highly nonlinear large-amplitude plasma wave and propagating for a long distance without significant spreading. The laser pulse can evolve into a state where its ponderomotive force causes electron density cavitation (which resembles a bubble). As the radially expelled electrons flow along the cavity boundary and collide at the bubble base, transverse breaking [29] occurs and a dense bunch of electrons are injected into the plasma wave. The trapped electron bunch produces a field that terminates further injection of electrons into the first bucket and damps the plasma wave behind the first bucket (beam loading), resulting in spatially and temporally localized injection and thus formation of a monoenergetic electron beam. In addition, the trapped electrons that are isolated in phase space will be further compressed in energy when they are accelerated to the maximum energy as the dephasing length is reached. If the plasma wave distribution is not terminated at this location, then the central electron energy will start to decrease and the energy spread will increase as the electrons enter the deceleration phase of the plasma wave [15,26].

Many works have been done to experimentally resolve the physical processes responsible for the production of the monoenergetic electron beam [12,30–33]. By using the laser machining technique [34,35], recently we have demonstrated tomographic measurements that resolve the injection and acceleration processes of the monoenergetic electron bunch [12]. In this paper, we present the tomographic method and the resolved injection and acceleration processes in detail, including a systematic investigation on the dependence of the characteristics of the monoenergetic electron beam on experimental parameters. The results are consistent with the model of transverse wave breaking and beam loading for injection of monoenergetic electrons [6–9,14–17,22–24]. This work also demonstrates the great potential of the tomographic method as a new diagnosis tool for laser-plasma interactions.

II. EXPERIMENTAL SETUP

A 10-TW, 45-fs, 810-nm, and 10-Hz Ti:sapphire laser system, upgraded from that reported in Ref. [36], is used for this

---

[*] URL: http://ltl.iams.sinica.edu.tw
[†] Electronic address: sychen@ltl.iams.sinica.edu.tw

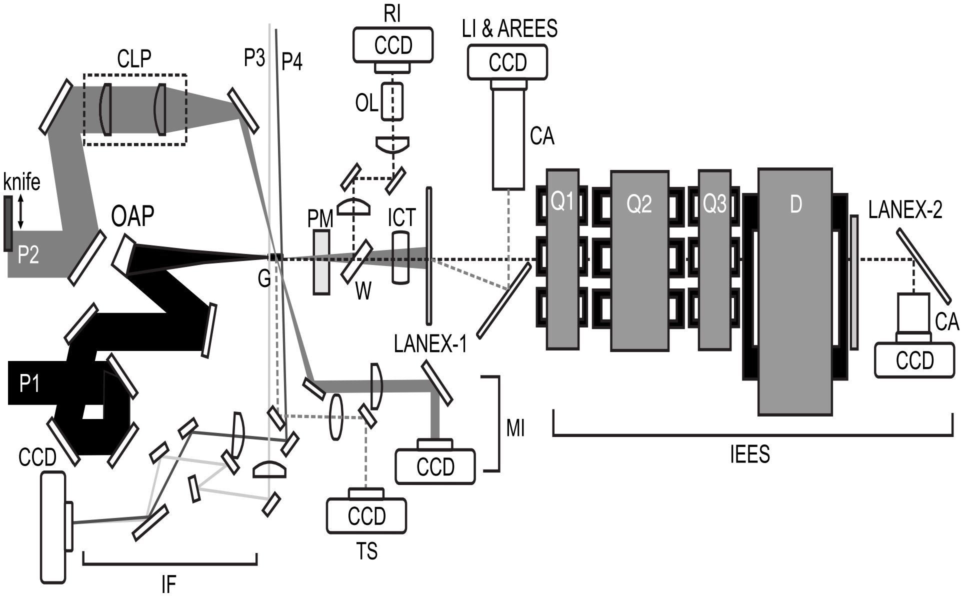

FIG. 1. Experimental layout (for clarity, the wall of the vacuum chamber is not shown). $P1$, pump pulse; $P2$, machining pulse; $P3$, probe pulse; $P4$, reference pulse; CLP, cylindrical lens pair; OAP, off-axis parabolic mirror; IF, interferometry imaging system; G, gas jet; PM, permanent magnet; RI, pump-pulse relayed imaging system; OL, objective lens; W, glass wedge; ICT, integrating current transformer; TS, Thomson scattering imaging system; LI & AREES, LANEX-1 imaging system and nonimaging angularly resolved electron-energy spectrometer; CA, camera lens; MI, machining-beam profile imaging system; $Q1-Q3$, quadrupole electromagnets; D, dipole electromagnet; IEES, imaging electron-energy spectrometer; CCD, charge-coupled device camera.

experiment. After the amplifier chain of the laser system the laser beam with a clear aperture of 4 cm diameter is split into two, each going through an energy tuner and a pulse compressor. One beam serves as the pump pulse for driving a plasma wave, and the other, set to be 7.5 ns earlier than the pump pulse, is used as the machining pulse for the tomographic measurement described in Sec. III. The temporal contrast of the laser pulses is measured to be about 10^6 at -50 ps and 10^4 at -1 ps.

Figure 1 shows the experimental layout. The pump pulse is focused by an $f/8$ off-axis parabolic mirror onto a gas jet. The focal spot has a 8-μm diameter in full width at half maximum (FWHM) with 80% energy enclosed in a Gaussian-fit profile, measured with a relayed imaging system. The pump-pulse peak intensity in vacuum is 5.6×10^{18} W/cm^2 for a 230-mJ, 45-fs pump pulse, corresponding to a laser strength parameter of $a_0 = 1.5$. The relayed imaging system is composed of a glass wedge, a pair of lenses with 300-mm focal length, an objective lens, and a charge-coupled device (CCD) camera. The first lens and the wedge are mounted on motorized stages so that the pump-pulse beam profiles at various positions can be imaged and the wedge can be removed out of the way to allow measurement of the electron beam.

The hydrogen gas jet is produced from a pulsed valve with a supersonic nozzle. Three different nozzles are used in this experiment. The first nozzle, with a round outlet, produces a 1-mm gas jet with a uniform-density region of 0.9-mm length and a slope of 200-μm length at both edges along the pump propagation direction. The second nozzle, with a rectangular outlet, produces a 2-mm gas jet with a uniform-density region of 1.4-mm length and a slope of 200-μm length at the front edge. The third nozzle, also with a rectangular outlet, produces a 5-mm gas jet with a uniform-density region of 4.4-mm length and a slope of 200-μm length at the front edge. For the latter two gas jets a mask is adhered to the entrance edge of the nozzle to sharpen the gas boundary. The widths of both gas jets are 600 μm.

The transverse profile of the electron beam is measured by a LANEX (Kodak) scintillating screen imaged by a CCD camera [37], referred to as LANEX-1 in Fig. 1. The LANEX-1 screen is covered with a 50-μm aluminum foil on the front face to block the laser light and electrons with energies below 200 keV and placed at 34 cm (unless specified otherwise) downstream behind the gas jet along the pump-pulse propagation direction. The absolute electron number measured with the LANEX-1 imaging system is calibrated by using an integrating current transformer (ICT) of known sensitivity. By putting a permanent magnet behind the gas jet to disperse the electron beam on the LANEX-1 screen, angularly resolved electron-energy spectra are obtained [37]. Both the permanent magnet and the LANEX-1 screen can be moved in or out of the way of the electron beam in vacuum.

Electron-energy spectra with higher accuracy and resolution are measured by using an imaging electron spectrometer composed of three quadrupole electromagnets, one dipole electromagnet, and a LANEX screen imaged by a CCD camera, which is referred to as LANEX-2 in Fig. 1. The LANEX-2 screen is covered with a 25-μm aluminum foil on the front face to block the laser light and electrons with energies below 100 keV. The electron beam propagates in vacuum through all the four electromagnets until it reaches the LANEX-2 screen which also plays the role of vacuum window. The quadrupoles image the electron beam from the position of the gas jet to the LANEX-2 screen so that the error in energy measurement that may arise from pointing fluctuation of the electron beam is greatly reduced. The effective lengths of the three quadrupole electromagnets ($Q1$, $Q2$, $Q3$) and the dipole electromagnet (D) are 10 cm, 15 cm, 10 cm, and 50 cm, respectively. When varying the field of the dipole electromagnet to measure the electron spectrum in a different range, the fields of the quadrupoles are tuned accordingly to maintain the imaging condition.

The propagation of the pump pulse in the plasma is observed by imaging Thomson scattering of laser light from plasma electrons. The direction of observation is in 90° polar angle and 18° azimuthal angle with respect to the pump-pulse propagation direction. A Mach-Zehnder interferometer is used to measure the plasma density distribution in the gas jet. The probe and reference beams, obtained by splitting from the output of the second-stage amplifier and compressed with a separate pulse compressor, have 40-μJ energy, 55-fs pulse duration, and 1-cm diameter. A polarizer with a contrast ratio of 10^4 is put in front of the CCD camera to eliminate the contamination in the interferogram image due to the scattering of the pump pulse.

III. TOMOGRAPHIC MEASUREMENTS BASED ON LASER MACHINING

The setup of the machining beam for the tomographic measurement is shown in Fig. 2(a) and the working principle is illustrated in Fig. 2(b). Propagating roughly perpendicularly to the pump pulse, the 60-mJ, 45-fs machining pulse is focused vertically by a cylindrical lens to 20-μm width and imaged horizontally by another cylindrical lens from the location of a knife onto the plane overlapping with the pump-pulse propagation path. In the vertical focusing, 80% energy is enclosed in a Gaussian-fit profile, and in the horizontal focusing 80% energy is enclosed in a Lorentzian-fit profile. For each nozzle used in the measurements, the length of the line focus of the machining pulse is varied to match with the length of the gas jet. This line focus overlaps with the propagation path of the pump pulse inside the gas jet and the intensity of the machining beam within the overlapped region exceeds the threshold of optical-field ionization. The purpose of the knife is to block part of the machining beam. In the part of the line focus not blocked by the knife, gas irradiated by the machining beam is ionized and heated. After 7.5 ns the region ionized by the machining beam is evacuated as a result of hydrodynamic expansion of plasma. In this way we can adjust the length of the interaction region by scanning the knife-edge position and measure the number and spectrum of accelerated electrons as functions of pump-pulse propagation distance. The spatial resolution of the tomography along the beam propagation direction is better than 20 μm, as shown by the boundary sharpness of the side scattering images [35]. Note that such a tomographic measurement cannot be accomplished by using a set of gas jet nozzles with various lengths, because the atomic density and density profile all change with nozzles. In that case it is difficult to vary the interaction length while keeping other parameters fixed.

Figure 3(a) shows the intensity distributions of the machining pulse in vacuum on the plane of pump-pulse propagation for various knife-edge positions. These intensity distributions are used in the experiment with the 1-mm gas jet. The interferograms of the plasma taken at 20 ps after the pump pulse traversing the gas jet with (4.0×10^{19})-cm^{-3} hydrogen atom density for various knife-edge positions are shown in Fig. 3(b). The plasma density distributions before and after the position of the knife-edge image are characteristically different. After retrieving the plasma density distribution from the interferograms, it is found that the on-axis plasma density in the unmachined region is the same as the hydrogen atom density while that in the machined region is greatly reduced. If a cylindrically symmetric plasma is assumed, the retrieved on-axis plasma density in the machined region is about 1/20 of the initial hydrogen atom density. However, since the Rayleigh length of the machining beam is much larger than the vertical width of the machining beam, the machined region should be of elliptical cross section. With the assumption of no plasma density variation along the probe direction, the retrieved on-axis plasma density is about 1/5 of the initial hydrogen atom density. There-

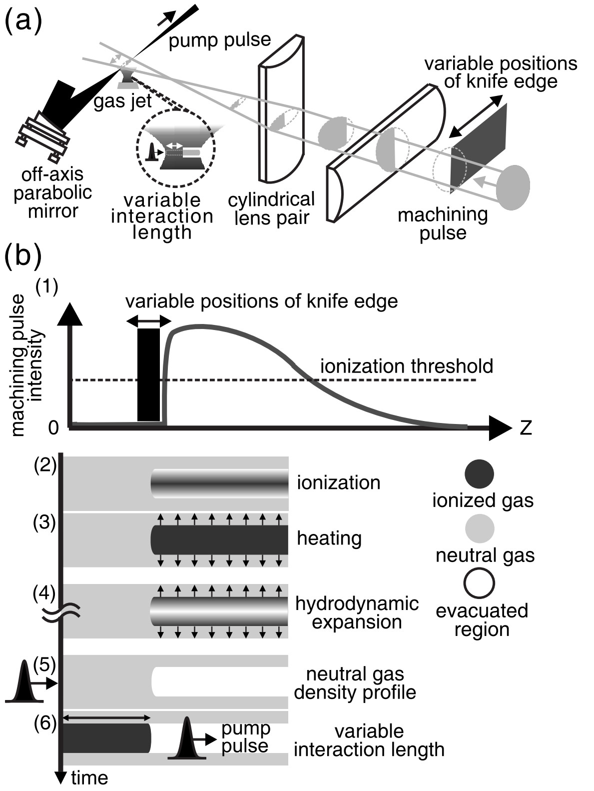

FIG. 2. (a) Setup of the machining beam. (b) Working principle for the tomographic measurement: (1) The laser intensity within the entire gas-jet length is set above the intensity threshold of optical-field ionization, and the boundary between the unirradiated and irradiated regions is set by the knife-edge position, (2) Plasma is formed only in the irradiated region, (3) The plasma is heated by the same machining pulse through above-threshold ionization heating and inverse bremsstrahlung heating, (4) The plasma expands outwards via hydrodynamic expansion, (5) After a long delay on the order of 10 ns, the plasma is almost completely evacuated, (6) When the pump pulse propagates through the gas jet, the actual interaction length is determined by the position of the knife edge.

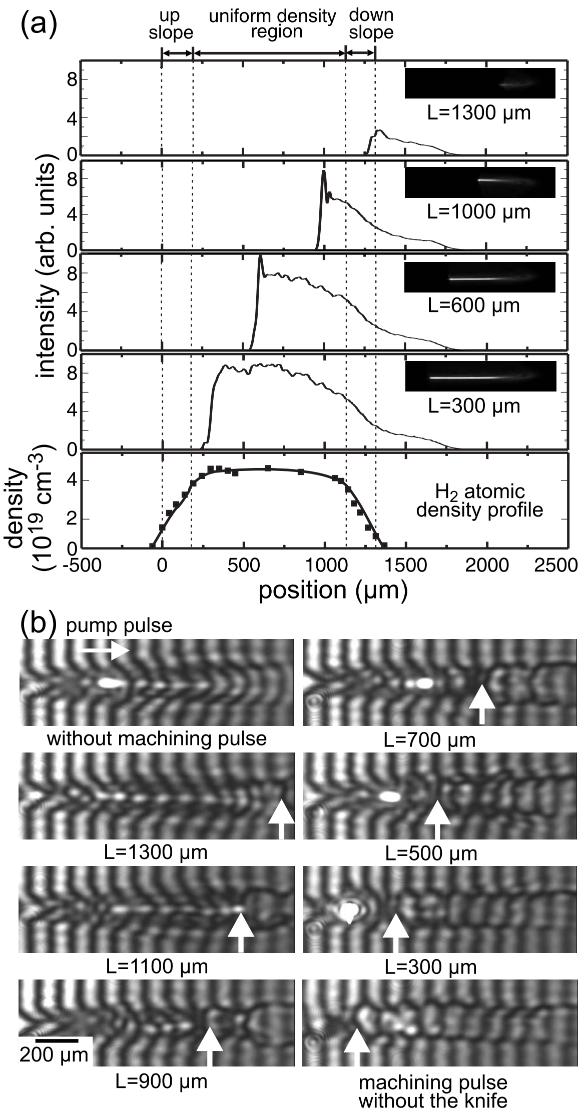

FIG. 3. (a) Line profiles and images of the machining-beam intensity distribution in the region of pump-pulse propagation for various knife-edge positions. The gas density distribution of the 1-mm gas jet is shown at the bottom graph for comparison. (b) Interferograms of the plasma taken at 20 ps after the 230-mJ, 45-fs pump pulse traversing the gas jet of (4.0×10^{19})-cm^{-3} hydrogen atom density for various knife-edge positions. The white arrows indicate the image position of the knife edge.

fore, the actual on-axis plasma density in the machined region should be smaller than 1/5 and larger than 1/20 of the initial atom density. In addition, the cross section of the reduced-density region is around 100 μm by 500 μm, which is determined by translating the position of the vertically focusing cylindrical lens in the two directions perpendicular to the pump-pulse propagation direction to observe the corresponding variation in the number of accelerated electrons. The dimension of 100 μm by 500 μm is consistent with that estimated from the interferograms shown in Fig. 3(b), for the vertical direction, and that estimated from the Rayleigh length of the machining beam, for the horizontal direction. In the machined region the pump-pulse intensity is much lower than that in the unmachined region, because the pump pulse cannot undergo relativistic self-focusing under such low plasma density. The machined density channel may act as a plasma waveguide [38]; however, in this condition the guided beam size is too large to support the intensity required for plasma wave excitation. The low plasma density and low laser intensity render the plasma wave excited by the pump pulse in the machined region insignificant for changing the characteristics of the electron beam produced in the unmachined region. To resolve the electron acceleration process, this is the key element for the tomographic measurement to work properly. With the current experimental setup, the maximum length of machining is 2 mm with 60-mJ machining-pulse energy.

The intensity of the machining beam used in our experiment is just slightly higher than the saturation intensity of ionization of the gas. The temperature acquired by the plasma electrons from the machining beam through inverse bremsstrahlung heating is low because of the short pulse duration. Therefore, the expanding plasma does not lead to collisional ionization of the surrounding neutral gas and thus no shock wave is formed. This is different from the case of plasma waveguide formation driven by a line-focused long-duration and high-energy heater pulse in which the expanding plasma leads to collisional ionization of surrounding neutral gas and formation of shock wave. The difference in plasma temperature is the reason why a longer time scale for plasma expansion is required in this experiment (4–10 ns) than that in the case of plasma waveguide driven by long heater pulse (1–2 ns). In the tomographic measurement, after the long delay the ionized gas expands to a much larger volume and thus the plasma density in the unmachined regions after ionization by the pump pulse is increased only by a small ratio, even smaller than the density fluctuation of the gas jet. This is supported by two observations in our experiment. First, when a stretched pump pulse is used as a longitudinal probe to observe the density structure produced by the machining beam via side imaging of Thomson scattering [35], no increase of side scattering intensity in the unmachined regions is observed. Second, the interferogram taken without the pump beam shows no discernible fringe shift. Both of them indicate that there is no significant increase of plasma density in the unmachined regions caused by the machining beam at the arrival time of the pump pulse. Therefore, the expansion of the plasma ionized by the machining beam in the longitudinal direction does not affect the tomographic measurement.

From Ref. [34] it may be expected that some electrons can be injected at the boundary between the unmachined region and the machined region when the pump pulse driving a plasma wave traverses it. However, this does not interfere with the tomographic measurement since there is basically no plasma wave afterwards to accelerate these electrons to significant energy.

IV. CHARACTERISTICS OF THE MONOENERGETIC ELECTRON BEAM

The inset of Fig. 4(a) shows the angular distribution of the electron beam produced by using only the pump pulse with

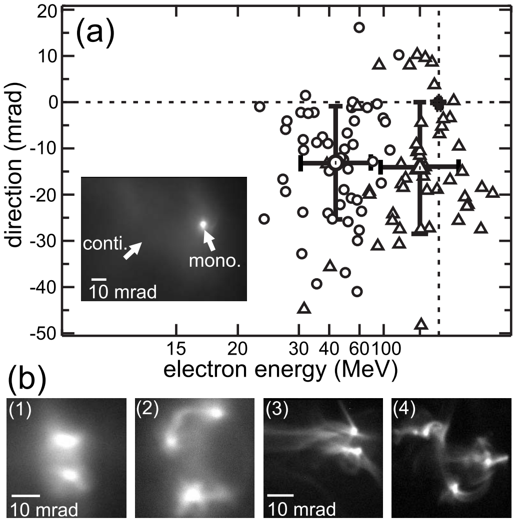

FIG. 4. (a) Pointing directions of the monoenergetic electron beam measured with the LANEX-1 imaging system with (open circles) and without (open triangles) the dispersing permanent magnet. The permanent magnet with 0.15-T magnetic field and 4-cm effective length is placed at 5 cm behind the gas jet, and the LANEX-1 screen is placed at 40 cm behind the gas jet. The inset shows the angular profile of the electron beam. The data are taken with the 2-mm gas jet, a hydrogen atom density of 4.0×10^{19} cm^{-3}, and a focal position of 200 μm. The pump pulse is 230 mJ in energy with a pulse duration of 45 fs. The error bars denote the standard deviation for 50 laser shots. The cross point of the two dash lines indicates the laser pointing direction in vacuum. (b) Angular profiles of the accelerated electron beam measured by the LANEX-1 imaging system for several unusual cases without (1, 2) and with (3, 4) the dispersing permanent magnet.

the 2-mm gas jet at a hydrogen atom density of 4.0×10^{19} cm^{-3} and a focal position of 200 μm behind the front edge of the gas jet. The pump pulse is 230 mJ in energy with a pulse duration of 45 fs. Two beam components appear in the electron beam: one has an angular divergence of ~4 mrad and the other has an angular divergence of ~50 mrad. Measurements using the nonimaging angularly resolved electron-energy spectrometer reveal that the electron beam with a smaller divergence has a quasi-monoenergetic energy spectrum and that with a larger divergence has an approximately Maxwellian energy distribution. The number of electrons in the monoenergetic electron beam is 1.4×10^9 and that in the continuum electron beam is 4×10^{10}. The fluctuation of number of electrons for the monoenergetic electron beam is about 43% in standard deviation for 20 samples (laser shots in which a monoenergetic electron beam appears), close to that reported by Faure *et al.* [6] and Leemans *et al.* [17]. Figure 4(a) shows the pointing directions of the monoenergetic electron beam measured with the LANEX-1 imaging system with and without the dispersing permanent magnet. The permanent magnet with a 0.15-T magnetic field and a 4-cm effective length is placed at 5 cm behind the gas jet, and the LANEX-1 screen is placed at 40 cm behind the gas jet. The pointing fluctuation of the monoenergetic electron beam is found to be about 8 mrad (horizontal) by 13 mrad (vertical) in standard deviation. With or without the permanent magnet, the pointing fluctuation is roughly the same. The pointing fluctuation may be due to fluctuation in the amplitude and phase of channel betatron oscillation [18,19,24], which originates from fluctuation in the injection by transverse wave breaking. Since the beam pointing fluctuation interferes with the electron energy measurement, the fluctuation in the electron energy shown in Fig. 4(a) is not the real energy fluctuation. By comparing the electron beam directions averaged over 50 laser shots with and without the magnet, the energy of the monoenergetic electron beam is measured to be around 45 MeV.

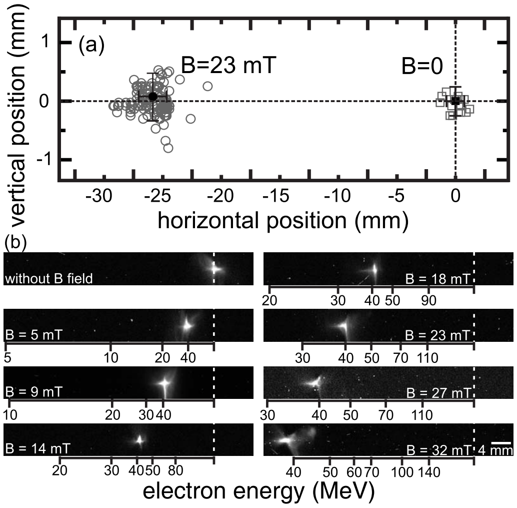

FIG. 5. (a) Positions of the monoenergetic electron beam on the LANEX-2 screen with (open circles) and without (open squares) turning on the dipole magnetic field of 23 mT in the imaging electron-energy spectrometer. The data are taken with the 2-mm gas jet, a hydrogen atom density of 4.0×10^{19} cm^{-3}, and a focal position of 200 μm. The pump pulse is 230 mJ in energy with a pulse duration of 45 fs. (b) Images on the LANEX-2 screen under the same experimental condition for various dipole magnetic fields. The quadrupole magnetic fields are varied in accordance with the dipole magnetic field to maintain a minimal spot size on the screen. The vertical dashed line indicates the position of the monoenergetic electron beam without the magnetic field.

Occasionally multiple bright spots in the electron beam are observed in the LANEX-1 imaging system without [(1) and (2) in Fig. 4(b)] and with [(3) and (4) in Fig. 4(b)] the dispersing magnet. Such a structure may be caused by simultaneous injection of many electron bunches into the first bubble at transverse wave breaking or by the injection of electrons in multiple bubbles (multiple plasma-wave buckets) [8].

Figure 5(a) shows the position of the monoenergetic electron beam on the LANEX-2 screen with and without the dipole magnetic field in the imaging electron-energy spectrometer under the same experimental condition of Fig. 4. The central energy of the monoenergetic electron beam is measured to be 43 MeV. With the quadrupole electromagnets the fluctuation of the horizontal position of the monoenergetic electron beam on the LANEX-2 screen due to the electron-beam pointing fluctuation is greatly reduced. The energy fluctuation of the monoenergetic electron beam pro-

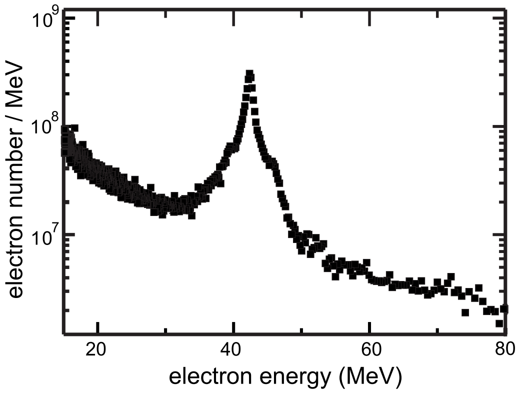

FIG. 6. Typical single-shot energy spectrum of the electron beam measured by the imaging electron-energy spectrometer. The data are taken with the 2-mm gas jet, a hydrogen atom density of 4.0×10^{19} cm^{-3}, and a focal position of 200 μm. The pump pulse is 230 mJ in energy with a pulse duration of 45 fs.

duced in this condition is measured to be ~9% in standard deviation for 127 samples in consecutive experimental runs. Figure 5(b) shows the images on the LANEX-2 screen under the same experimental condition of Fig. 4 for various dipole magnetic fields. The quadrupole magnetic fields are varied in accordance with the dipole magnetic field to maintain a minimal spot size on the screen. The electron energy measured by this spectrometer is about the same regardless of the different magnetic fields used, as it should be for a well-functioning spectrometer.

Figure 6 shows a typical single-shot energy spectrum of the electron beam under the same experimental condition of Fig. 4, measured with a dipole magnetic field of 14 mT. For the monoenergetic electron beam the central energy, the energy spread in FWHM and the ratio between them are about 42 MeV, 1.3 MeV, and 3%, respectively. However, the actual energy spread should be smaller than 3% because the resolution of this spectrometer is limited by the spot size of the monoenergetic electron beam on the LANEX-2 screen. Improvement in the resolution of energy spread measurement will be done by adding an extension chamber so that the LANEX-2 screen can be moved further away from the exit face of the dipole electromagnet. From the measured electron number and energy it is estimated that the total energy contained in the monoenergetic electron beam is about 10 mJ and the energy conversion efficiency from laser to monoenergetic electrons is about 5%. The average energy of the continuum electron beam is only about 3.5 MeV and thus the efficiency of energy conversion from the laser pulse to the continuum electron beam is about 10%. Therefore, the efficiency of energy conversion from the laser pulse to the whole electron beam is about 15%, which is somewhat larger than the 10% energy conversion efficiency reported by Faure *et al.* [6]. The higher energy conversion efficiency can be ascribed to the much higher plasma density in our experiment, even though the laser peak power is lower.

The energy fluctuation of the monoenergetic electron beam reported by Mangles *et al.* [8] for a 70-MeV electron beam is about 30% and that reported by Geddes *et al.* [15] for an 86-MeV electron beam is about 15%. In comparison, our results show a smaller energy fluctuation of 9%. The origin of the energy fluctuation of the monoenergetic electron beam may be ascribed to the fluctuations in the energy, pulse duration, and spot size of the pump pulse, since the bubble-regime acceleration is a highly nonlinear process that involves longitudinal compression and transverse self-focusing. Mangles *et al.* [8] ascribed the 30% energy fluctuation in their results to the ±5% fluctuation in laser pulse energy, ±12% fluctuation in pulse duration, and ±11% fluctuation in focal spot size. In contrast, the fluctuation in the laser parameters of the laser system used for this experiment is 1.3% in laser pulse energy, 2.4% in pulse duration, and 2.4% in focal spot size [36]. Therefore, it is reasonable that the energy fluctuation of the monoenergetic electron beam in our experiment is smaller. The fluctuation in electron number may be triggered by a certain instability. However, once the electrons are injected, the final output energy of the monoenergetic electron beam is mainly determined by the way the laser pulse evolves.

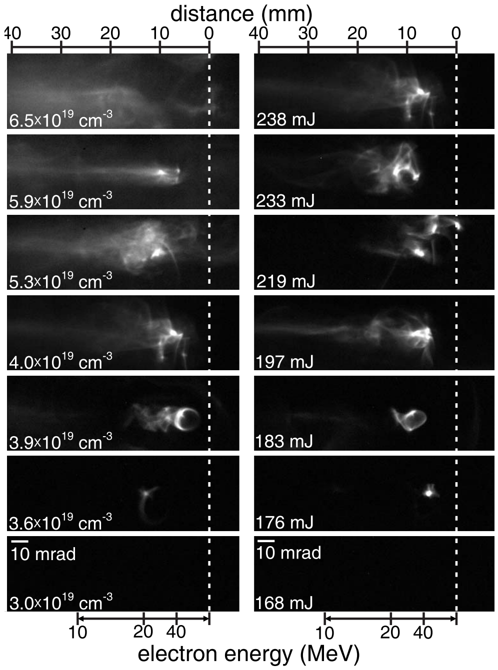

FIG. 7. Typical images of the electron beam recorded with the nonimaging angularly resolved electron-energy spectrometer (LANEX-1 screen) for various pump-pulse energies at 4.0×10^{19}-cm^{-3} plasma density and various plasma densities at 230-mJ pump-pulse energy with the 2-mm gas jet. The pump-pulse duration is 45 fs and the pump focus position is at 200 μm. The permanent magnet used has 0.15-T magnetic field and 2-cm effective length, and it is placed at 4 cm after the gas jet. The vertical dashed line indicates the average position of the monoenergetic electron beam without the magnetic field.

V. PARAMETER SPACE FOR THE PRODUCTION OF MONOENERGETIC ELECTRON BEAM

Figures 7 and 8 show the typical images of the electron beam recorded with the nonimaging angularly resolved electron-energy spectrometer (LANEX-1 screen) for various

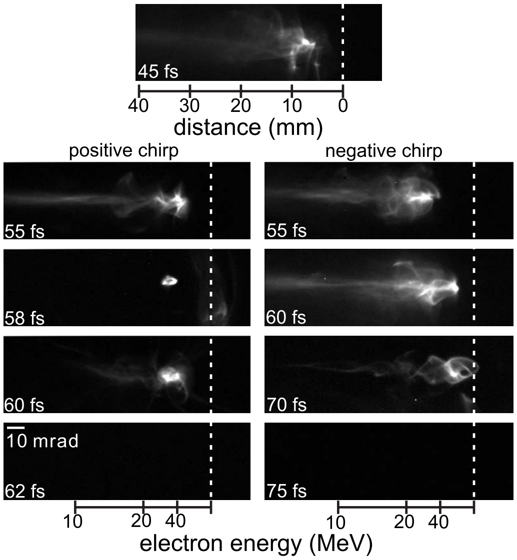

FIG. 8. Typical images of the electron beam recorded with the nonimaging angularly resolved electron-energy spectrometer (LANEX-1 screen) for various pump-pulse duration and chirp. The data are taken with the 2-mm gas jet, a hydrogen atom density of 4.0×10^{19} cm^{-3}, and a focal position of 200 μm. The pump pulse is 230 mJ in energy. The permanent magnet used has 0.15-T magnetic field and 2-cm effective length, and it is placed at 4 cm after the gas jet. The vertical dashed line indicates the average position of the monoenergetic electron beam without the magnetic field.

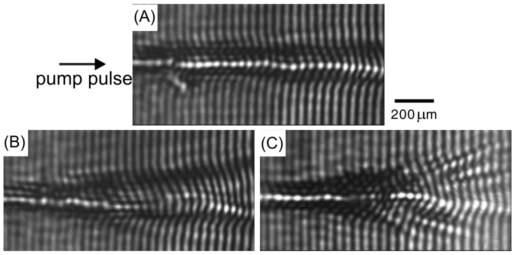

FIG. 9. Typical interferograms of the plasma taken at 20 ps after the 230-mJ, 45-fs pump pulse traversing the 1-mm gas jet of (4.0×10^{19})-cm^{-3} plasma density for various temporal contrasts. From (a) to (c) the prepulse level is increased by detuning the pump timing of the laser amplifiers.

pump-pulse energies, plasma densities, and pump-pulse durations and chirps, respectively. The measurements are done using the 2-mm gas jet. At a pulse duration of 45 fs and a plasma density of 4.0×10^{19} cm^{-3}, the monoenergetic electron beam appears when the pump-pulse energy exceeds $\sim$170 mJ. At a fixed pump-pulse energy of 230 mJ and a fixed plasma density of 4.0×10^{19} cm^{-3}, the monoenergetic electron beam disappears when the pump-pulse duration exceeds 70 fs. These two observations seem to indicate that self-injection of the monoenergetic electron beam can occur as long as the peak power of the incident pump pulse exceeds a threshold ($\sim$3 TW), regardless of the ratio of the pump-pulse duration to the plasma-wave period. In the regime where the pump-pulse duration is longer than the plasma-wave period, self-modulational instability can break up the pump pulse into a pulse train with the pulse duration matching the plasma-wave period. After that, self-focusing and longitudinal compression of these pulses can lead to excitation of a few plasma bubbles as described by the bubble-regime model. The bubble that first evolves to the shape that can induce transverse wave breaking may dominate the observed monoenergetic electron bunch. Therefore, that the initial pump-pulse duration must be shorter than the plasma-wave period may not be a strict requirement for producing a self-injected monoenergetic electron beam [8,26], and our experimental data support this point.

As the plasma density is varied at a fixed pump-pulse energy of 230 mJ and a fixed pulse duration of 45 fs, the monoenergetic electron beam appears only in the range of $3.3\times10^{19}-6.2\times10^{19}$ cm^{-3}. Below the lower limit both the monoenergetic electron beam and the continuum electron beam vanish. Above the upper limit the monoenergetic electron beam vanishes while the electron number of the continuum electron beam increases. The thresholds of pulse duration, pulse power, and plasma density for the production of the monoenergetic electron beam suggest that self-focusing seems to play a crucial role in the production of the monoenergetic electron beam, which is consistent with the model of injection by transverse wavebreaking in the bubble regime. For various plasma densities, the ratio of the pump-pulse peak power to the critical power $P_c=17(\omega_0^2/\omega_p^2)$ GW [3], where ω_0 is the laser frequency and ω_p is the plasma frequency, must be in the range of 3.4–8.8 in order to produce the monoenergetic electron beam. Such an observed range of P/P_c is consistent with the results reported by other groups [6–8,10,13]. In this experiment, we did not observe a significant dependence of the parameters of the electron beam on the sign of laser pulse chirp. This is consistent with the observations reported previously that chirp has no significant effect on relativistic self-guiding [39] and Raman forward-scattering instability [40] under our experimental condition.

Under the optimal condition the probability of appearance of the monoenergetic electron beam is about 80%. It seems that the pre-ionization front produced by the pedestal of the pump beam plays a nontrivial role in determining the appearing probability of the monoenergetic electron beam. It is observed that the probability goes down when the temporal contrast is reduced by detuning the pump timing of the laser amplifiers. Figure 9 shows the corresponding interferograms of the plasma taken at 20 ps after the 230-mJ, 45-fs pump pulse traversing the 1-mm gas jet of (4.0×10^{19})-cm^{-3} plasma density for various temporal contrasts. As shown, better self-guiding is achieved when the laser temporal contrast is increased. In addition, it is found that the appearing probability decreases when the steepness of the front slope of the gas jet is reduced. According to the observations in the past [37,39], the quality of self-guiding is also better when the front slope of the gas jet is steeper. These two observations again support the correlation between the production of the monoenergetic electron beam and self-focusing or self-channeling. The origin of the probabilistic nature in the appearance of the monoenergetic electron bunch is believed to result from fluctuations in the transverse wave breaking due to fluctuations in the evolution of the pump pulse. In such highly nonlinear process, even a small shot-to-shot fluctuations in laser beam profile, temporal shape, or pulse energy may have an observable influence on the transverse wave breaking.

VI. TOMOGRAPHY OF THE INJECTION AND ACCELERATION PROCESSES

Tomographic measurements are carried out by using the laser machining technique in conjunction with various diagnoses for the electron beam. Figures 10(a) and 10(b) show the central energy of the monoenergetic electron beam and the typical energy spectrum, respectively, as functions of position in the 2-mm gas jet measured by the imaging electron-energy spectrometer. The pump pulse is 230 mJ in energy with a pulse duration of 45 fs, the plasma density is 4.0×10^{19} cm^{-3}, and the pump-pulse focal position is at 200 μm behind the front edge of the gas jet. As shown in Fig. 10(a), the central energy of the monoenergetic electron beam increases roughly linearly from 6.2 MeV at the position of 550 μm to 42.7 MeV at the position of 700 μm, corresponding to an acceleration gradient of 2.4 GeV/cm. The tomography technique provides a direct measurement of the electron acceleration gradient in a laser-plasma-based electron accelerator. Previously the electron acceleration gradient was calculated from the final energy of the electron beam divided by the interaction length estimated from side images of Thomson scattering or the gas-jet length, both of which over estimated the true acceleration distance as revealed by the direct tomographic measurement.

According to the one-dimensional theory [3], at (4.0×10^{19})-cm^{-3} plasma density the dephasing length is 220 μm and the nonrelativistic wave-breaking limit is 6 GV/cm. The acceleration gradient measured in this experiment is 2.4 GV/cm, corresponding to a plasma-wave amplitude of 40%. In comparison, the plasma-wave amplitude calculated using one-dimensional standard laser-wakefield theory at resonant pulse duration is about 85%. The dephasing energy calculated using 40% plasma-wave amplitude is about 56 MeV. It seems that all these parameters measured except the plasma-wave amplitude are close to that calculated with one-dimensional theory. However, the three-dimensional nature of the bubble-regime model makes accurate comparison with simple one-dimensional theory less meaningful.

As shown in Fig. 10(a), the energy of the monoenergetic electron beam reaches a maximum after the position of 700 μm and stays at the same value for the rest part of the 2-mm gas jet. The observation of energy saturation in the monoenergetic electron beam is also supported by the measurement with the 5-mm gas jet under the same experimental condition. In that case the output energy of the monoenergetic electron beam is ~41 MeV, which is close to that with the 2-mm gas jet regardless of the great extension of the gas-jet length. According to previous theories the accelerated electrons should enter the deceleration region of the plasma wave after the dephasing length and start to lose energy, instead of staying at a saturation value. In contrast, our observation seems to indicate that in our experiment the plasma wave is terminated or becomes incoherent after an acceleration distance of 150 μm such that the electrons are not affected afterwards. The termination or breaking up of the plasma wave at a distance after entering the bubble regime may be caused by catastrophic evolution of the pump pulse or by a prepulse in the pump beam that preforms a density inhomogeneity in the propagation path to break up the propagation of the main pump pulse [41]. It can be noted that the

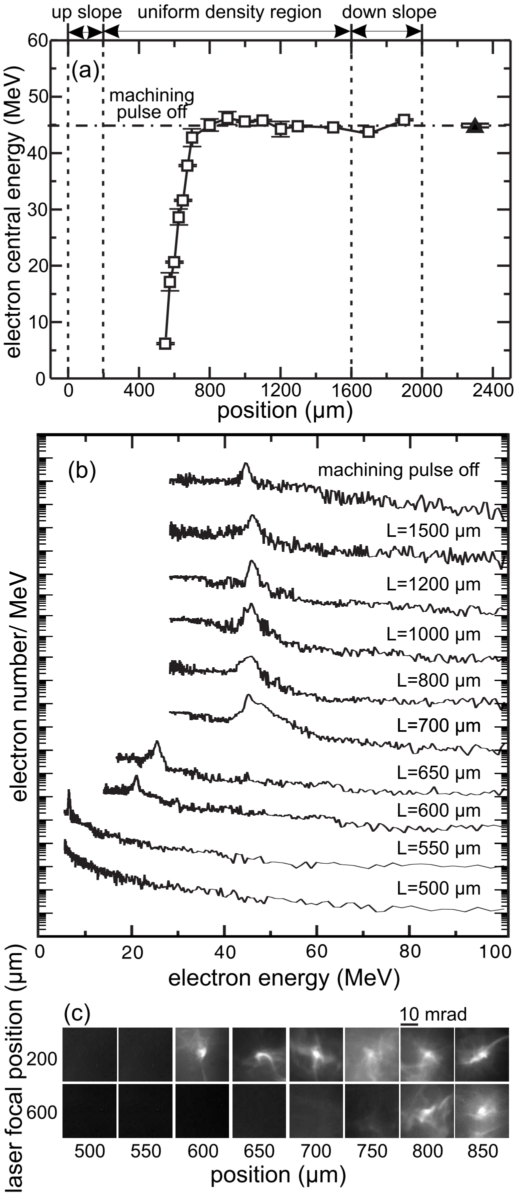

FIG. 10. Central energy (a) and typical energy spectrum (b) of the monoenergetic electron beam, respectively, as functions of position in the 2-mm gas jet measured by the imaging electron-energy spectrometer. The pump pulse is 230 mJ in energy with a pulse duration of 45 fs, the plasma density is 4.0×10^{19} cm^{-3}, and the pump-pulse focal position is at 200 μm. The error bars represent the standard error of mean over 15 laser shots. The energy spectrum for the case of no machining pulse is also shown for comparison. The vertical scale is a logarithmic scale and each spectrum is offset vertically to prevent overlap. (c) Typical images of the electron beam on the LANEX-1 screen for various interaction lengths set by the knife-edge position with pump-pulse focal positions of 200 μm and 600 μm, respectively.

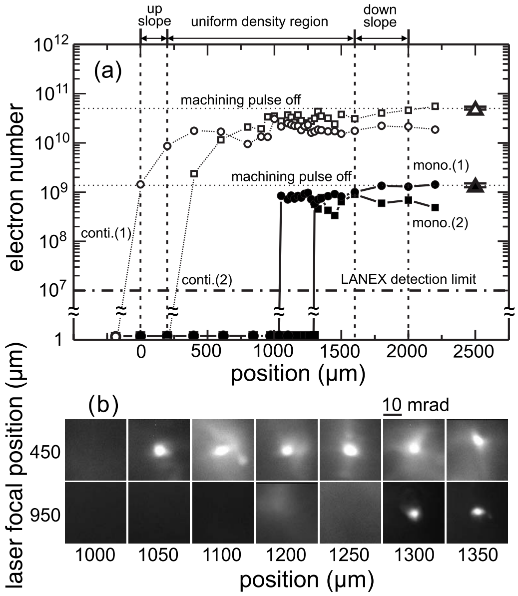

FIG. 11. Numbers of electrons in the monoenergetic electron beam and the continuum electron beam as functions of position in the gas jet (a) and the corresponding typical electron beam profile images (b) for pump-pulse focal positions of 450 μm, (1), and 950 μm, (2), respectively. The data are taken under the same condition as for Fig. 10 except that the focal-spot diameter of the pump pulse is 11 μm. The error bars represent the standard error of mean over 10 laser shots (for squares and circles) or 20 laser shots (for triangles).

saturation energy in Fig. 10(a) is equal to the electron energy measured without the machining beam and there is no variation of electron energy after the saturation position arising from the effects of the plasma wave excited in the machined region. Both of these two facts verify that the tomographic measurement is working properly.

Figure 10(b) also provides information on the evolution of energy spread of the monoenergetic electron beam after the injection position. Although the resolution of energy spread is limited by the spot size of the electron beam on the LANEX-2 screen, it can be seen that the monoenergetic electron beam has already acquired a finite energy spread since its injection and stays so during the acceleration. This indicates the energy compression that occurs when the electrons approach the dephasing length is not a necessary condition for the production of a monoenergetic electron beam, even though it may help reduce the energy spread.

Figure 10(c) shows the typical images of the electron beam on the LANEX-1 screen for various interaction lengths set by the knife-edge position with pump-pulse focal positions of 200 μm and 600 μm, respectively. By integrating the intensity of the images of the monoenergetic electron beam component and the continuum electron beam component separately, the numbers of electrons for these two components are measured as functions of position in the gas jet. From the data in Fig. 10(c), the data in Fig. 11 which are taken with a different set of focal positions and focal spot size, and the data in Ref. [12], it is consistently found that the injection of continuum electrons starts at an earlier position and continues along with the propagation of the pump pulse. In contrast, the monoenergetic electron beam is injected at a later position along the propagation path and no further injection occurs afterwards. For each pump-pulse focal position all the monoenergetic electrons are found to be injected at the same spatial position, and right after their injection the number of continuum electrons ceases to increase. These observations are consistent with the bubble-regime model, in which monoenergetic electrons are injected by transverse wave breaking only after the laser pulse has evolved to a particular three-dimensional shape by self-focusing and longitudinal compression, and once the injection occurs the beam loading effect inhibits further injection of both the monoenergetic electrons and the continuum electrons. The production of the continuum electrons can be ascribed to the injection of electrons into the plasma wave by Raman backward-scattering instability [42,43]. The acceleration of continuum electrons should damp the plasma wave, which leads to a longer distance required for the laser pulse to evolve to the status for inducing transverse wave breaking and thus injection of monoenergetic electrons.

Figure 10(c) also shows the dependence of the position of injection of the monoenergetic electron beam on the focal position of the pump pulse. The injection position is shifted from 600 μm to 800 μm when the pump-pulse focal position is moved from 200 μm to 600 μm. Figure 11(a) shows the numbers of electrons in the monoenergetic electron beam and the continuum electron beam as functions of position in the gas jet, and Fig. 11(b) shows the corresponding electron beam profile images. The data in Fig. 11 are taken with a larger pump-pulse focal-spot size of 11 μm in diameter. The injection position of the monoenergetic electron beam is shifted from 1050 μm to 1300 μm when the pump-pulse focal position is moved from 450 μm to 950 μm. These results indicate that the position of injection of the monoenergetic electron beam shifts downstream when the pump-pulse focus is moved deeper into the gas jet, and the injection occurs at an earlier position when a smaller pump-pulse focal spot is used. Such observations are consistent with the bubble-regime model, since both the focal position in the gas jet and the size of the focal spot should affect how fast the laser pulse evolves to the specific shape for inducing transverse wave breaking and thus injection of the monoenergetic electron bunch. With the pump-pulse focus positioned at roughly the beginning of the uniform-density region, the distance of pump-pulse propagation for inducing the injection of monoenergetic electrons is about 400–700 μm. This distance is consistent with that observed in the three-dimensional particle-in-cell simulations with a laser pulse duration longer than the plasma-wave period in a bare gas jet [26]. It is also noted that the output energy of the monoenergetic electron beam is about the same for different pump-pulse focal spot positions. This result seems to indicate that there is little difference in the evolution of the plasma bubble after the position of onset of transverse wave breaking, although it takes different time to evolve into this state for different focal spot positions.

VII. SUMMARY

In summary, we have carried out a detailed investigation on the production of a monoenergetic electron beam in a self-injected laser-wakefield accelerator. A tomographic method based on laser machining is developed to resolve the injection and acceleration processes. With this method we are able to measure the true acceleration gradient directly, which is significantly larger than the value obtained by indirect measurements. It is found that the acceleration distance is only 150–200 μm in our experiments, and the electron energy saturates long before reaching the end of the plasma column. No deceleration is observed beyond the point of saturation, where the plasma wave and/or the driving laser pulse may have evolved into a catastrophically unstable state.

The injection of the monoenergetic electrons occurs a few hundred micrometers later than the starting point for the injection of the continuum electrons. All the monoenergetic electrons are injected at the same location, and at that point the injection of the continuum electrons stops. Right after the injection, the monoenergetic electrons acquire a narrow energy spectrum and remain so toward the end of acceleration. All the experimental data are consistent with the bubble-regime model, and the beam diagnoses and power threshold verify the important role of self-focusing or self-channeling in the production of monoenergetic electrons.

As we have demonstrated also in the study of high-order harmonic generation [44] and soft x-ray lasers [45], the tomographic method adds a new dimension to the diagnosis of laser-plasma interactions. With this method, effects that are accumulated in the longitudinal direction can be resolved by measuring them differentially with an increasing interaction length. When this method is combined with the frequency-domain holography [46], even the most difficult measurement on the spatiotemporal evolution of plasma wave can be achieved.

The method can also be used to analyze the evolution of the pump pulse in laser-plasma interactions by replacing the electron diagnoses with optical diagnoses, such as relayed imaging systems and optical spectrometers. With sufficient machining beam energy to produce a machined region of a larger diameter, tomographic measurement of the pump-pulse beam profile at various positions along the pump propagation direction can be achieved by keeping the imaging plane of a relayed imaging system at the boundary between the unmachined region and the machined region while scanning the knife edge. In this case the tomographic resolution will be determined by both the sharpness of the boundary between the machined and unmachined region and the depth of field of the imaging system. By using an optical spectrometer, the process of longitudinal compression of the pump pulse can also be analyzed. Such measurements, to be performed in the near future, will provide further insight into the underlying physics of monoenergetic injection and energy saturation in self-injected laser-wakefield accelerators.

ACKNOWLEDGMENT

This work was supported by the Program for Promoting Academic Excellence of Universities (Phase II) under Contract No. NSC 94-2752-M-194-001-PAE.

---

[1] T. Tajima and J. M. Dawson, Phys. Rev. Lett. **43**, 267 (1979).
[2] T. Katsouleas, Phys. Plasmas **13**, 055503 (2006).
[3] E. Esarey, P. Sprangle, J. Krall, and A. Ting, IEEE Trans. Plasma Sci. **24**, 252 (1996).
[4] V. Malka *et al.*, Science **298**, 1596 (2002).
[5] S. P. D. Mangles *et al.*, Phys. Rev. Lett. **94**, 245001 (2005).
[6] J. Faure *et al.*, Nature (London) **431**, 541 (2004).
[7] V. Malka *et al.*, Phys. Plasmas **12**, 056702 (2005).
[8] S. P. D. Mangles *et al.*, Nature (London) **431**, 535 (2004).
[9] K. Krushelnick *et al.*, Phys. Plasmas **12**, 056711 (2005).
[10] E. Miura *et al.*, Appl. Phys. Lett. **86**, 251501 (2005).
[11] A. Yamazaki *et al.*, Phys. Plasmas **12**, 093101 (2005).
[12] C.-T. Hsieh *et al.*, Phys. Rev. Lett. **96**, 095001 (2006).
[13] B. Hidding *et al.*, Phys. Rev. Lett. **96**, 105004 (2006).
[14] C. G. R. Geddes *et al.*, Nature (London) **431**, 538 (2004).
[15] C. G. R. Geddes *et al.*, Phys. Plasmas **12**, 056709 (2005).
[16] C. G. R. Geddes *et al.*, Phys. Rev. Lett. **95**, 145002 (2005).
[17] W. P. Leemans *et al.*, Nat. Phys. **2**, 696 (2006).
[18] A. Rousse *et al.*, Phys. Rev. Lett. **93**, 135005 (2004).
[19] K. T. Phuoc *et al.*, Phys. Plasmas **12**, 023101 (2005).
[20] K. K. Kainz *et al.*, Med. Phys. **31**, 2053 (2004).
[21] C. Chiu *et al.*, Med. Phys. **31**, 2042 (2004).
[22] A. Pukhov and J. Meyer-ter-vehn, Appl. Phys. B: Lasers Opt. **74**, 355 (2002).
[23] F. S. Tsung *et al.*, Phys. Rev. Lett. **93**, 185002 (2004).
[24] I. Kostyukov, A. Pukhov, and S. Kiselev, Phys. Plasmas **11**, 5256 (2004).
[25] S. Gordienko and A. Pukhov, Phys. Plasmas **12**, 043109 (2005).
[26] F. S. Tsung *et al.*, Phys. Plasmas **13**, 056708 (2006).
[27] W. Lu *et al.*, Phys. Rev. Lett. **96**, 165002 (2006).
[28] W. Lu *et al.*, Phys. Plasmas **13**, 056709 (2006).
[29] S. V. Bulanov *et al.*, Phys. Rev. Lett. **78**, 4205 (1997).
[30] J. Faure *et al.*, Phys. Rev. Lett. **95**, 205003 (2005).
[31] J. Faure *et al.*, Phys. Plasmas **13**, 056706 (2006).
[32] S. P. D. Mangles *et al.*, Phys. Rev. Lett. **96**, 215001 (2006).
[33] C. D. Murphy *et al.*, Phys. Plasmas **13**, 033108 (2006).
[34] T.-Y. Chien *et al.*, Phys. Rev. Lett. **94**, 115003 (2005).
[35] C.-H. Pai *et al.*, Phys. Plasmas **12**, 070707 (2005).
[36] H.-H. Chu *et al.*, Appl. Phys. B: Lasers Opt. **79**, 193 (2004).
[37] R. Wagner, S.-Y. Chen, A. Maksimchuk, and D. Umstadter, Phys. Rev. Lett. **78**, 3125 (1997).
[38] P. Volfbeyn, E. Esarey, and W. P. Leemans, Phys. Plasmas **6**, 2269 (1999).
[39] T.-W. Yau *et al.*, Phys. Plasmas **9**, 391 (2002).
[40] W. P. Leemans *et al.*, Phys. Rev. Lett. **89**, 174802 (2002).
[41] T.-Y. Chien *et al.*, Phys. Plasmas **11**, 1173 (2004).
[42] W.-T. Chen *et al.*, Phys. Rev. Lett. **92**, 075003 (2004).
[43] D. F. Gordon *et al.*, Phys. Rev. E **64**, 046404 (2001).
[44] C.-H. Pai *et al.*, Opt. Lett. **31**, 984 (2006).
[45] M.-C. Chou *et al.*, Phys. Rev. A **74**, 023804 (2006).
[46] N. H. Matlis *et al.*, Nat. Phys. **2**, 749 (2006).